

High-entropy electrolytes for practical lithium metal batteries

Received: 28 October 2022

Accepted: 17 May 2023

Published online: 6 July 2023

 Check for updates

Sang Cheol Kim^{1,6}, Jingyang Wang^{1,6}, Rong Xu¹, Pu Zhang¹, Yuelang Chen², Zhuojun Huang¹, Yufei Yang¹, Zhiao Yu², Solomon T. Oyakhire³, Wenbo Zhang¹, Louisa C. Greenburg¹, Mun Sek Kim³, David T. Boyle², Philaphon Sayavong², Yusheng Ye¹, Jian Qin³, Zhenan Bao³ & Yi Cui^{1,4,5} ✉

Electrolyte engineering is crucial for improving battery performance, particularly for lithium metal batteries. Recent advances in electrolytes have greatly improved cyclability by enhancing electrochemical stability at the electrode interfaces, but concurrently achieving high ionic conductivity has remained challenging. Here we report an electrolyte design strategy for enhanced lithium metal batteries by increasing the molecular diversity in electrolytes, which essentially leads to high-entropy electrolytes. We find that, in weakly solvating electrolytes, the entropy effect reduces ion clustering while preserving the characteristic anion-rich solvation structures, which is characterized by synchrotron-based X-ray scattering and molecular dynamics simulations. Electrolytes with smaller-sized clusters exhibit a twofold improvement in ionic conductivity compared with conventional weakly solvating electrolytes, enabling stable cycling at high current densities up to 2C (6.2 mA cm⁻²) in anode-free LiNi_{0.6}Mn_{0.2}Co_{0.2} (NMC622)||Cu pouch cells. The efficacy of the design strategy is verified by performance improvements in three disparate weakly solvating electrolyte systems.

Following the discovery of the Li||TiS₂ battery chemistry by Whittingham in the 1970s¹, the Li metal anode has been sought after for its high theoretical capacity and low redox potential^{2,3}. However, its problems in safety and cycle life led to the development of carbonaceous anodes that are now the commercially dominant anode technology⁴. Three decades after the first commercialization of lithium ion batteries, lithium metal batteries have been revitalized as a viable technology² with the aid of nanoengineering^{2,5}, solid electrolytes^{6,7} and particularly liquid electrolyte engineering^{8–15}. Novel liquid electrolytes including localized-high-concentration electrolytes (LHCEs) and single-salt single-solvent electrolytes have dramatically improved stability with Li metal anodes and high-voltage cathodes³.

Solvation has proven to be central to the stabilization of liquid electrolytes for Li metal batteries. Through molecular design and the use of highly fluorinated co-solvents, weakly solvating electrolytes with anion-rich Li⁺ solvation structures have achieved superior electrochemical stability at the high-voltage cathode and Li metal anode interfaces, prolonging the battery cycle life^{9–11,16,17}. However, most weakly solvating electrolytes show compromised ionic conductivities compared with conventional carbonate and ether electrolytes^{8,10,17–27} (Supplementary Fig. 1 and Supplementary Table 1), limiting the battery's high-rate cycling capabilities (Supplementary Fig. 2 and Supplementary Table 2)^{9,10,13,21,28–32}. An interesting finding is that weakly solvating electrolytes with comparable salt concentrations show similar viscosities

¹Department of Materials Science and Engineering, Stanford University, Stanford, CA, USA. ²Department of Chemistry, Stanford University, Stanford, CA, USA. ³Department of Chemical Engineering, Stanford University, Stanford, CA, USA. ⁴Department of Energy Science and Engineering, Stanford University, Stanford, CA, USA. ⁵Stanford Institute for Materials and Energy Sciences, SLAC National Accelerator Laboratory, Menlo Park, CA, USA. ⁶These authors contributed equally: Sang Cheol Kim, Jingyang Wang. ✉e-mail: yicui@stanford.edu

to conventional electrolytes, implying that viscosity is unlikely to be the driver of the discrepancies in conductivity (Supplementary Fig. 1). As will be discussed extensively in this study, we hypothesize that conductivities are intricately related with mesoscopic solvation structures including Li^+ clusters. Increased clustering of ions owing to poor ion dissociation in weakly solvating electrolytes^{33,34} is expected to increase the hydrodynamic radius and hinder transport²⁰. These weakly solvating electrolytes that form ion clusters often possess improved electrochemical stability but at the cost of ion conductivity, while strongly solvating electrolytes tend to have high conductivity but poor stability, implying a trade-off in tuning solvation strength (Fig. 1a).

While many strategies have relied on tuning the enthalpic interactions between Li^+ and its surrounding species^{8,10,12,15,17,21}, entropy (S) as a design knob has largely gone unnoticed for liquid electrolytes. We conjecture that we can modulate the solvation behaviour of weakly solvating electrolytes by tuning solvation entropy (Fig. 1b), defined as the change in entropy upon solvation of Li^+ from vacuum to solution. Increasing solvation entropy can decrease the free energy of solvation without changing solvation enthalpy, leading to improved ion dissociation and smaller ion clusters. Entropy has been leveraged in many other systems to improve materials properties. In high-entropy alloys and ceramics, entropic driving forces are exploited to modulate structure and phase behaviour³⁵. In these systems, the presence of a large number of components increases the configurational entropic contribution to the free energy, thereby suppressing ordering in favour of mixing³⁶. By utilizing this design principle, unexpected properties that surpass the averaged properties of the components can be attained³⁷. The high-entropy design concept has been applied to catalysts, thermoelectrics, corrosion-resistant materials and battery materials^{35,37}, such as novel battery cathodes^{36,38} and solid electrolytes³⁹ with superior electrochemical properties.

In this Article, we apply the high-entropy concept to weakly solvating liquid electrolytes to improve ion transport capabilities without compromising stability with high-voltage cathodes and Li metal anodes (Fig. 1b and Supplementary Fig. 5). We design high-entropy electrolytes (HEEs) with increased solvation entropy by increasing molecular diversity (Fig. 1c). HEEs are shown to have a twofold increase in ionic conductivity and can stably cycle up to 2C (-6.2 mA cm^{-2}), charging and discharging in high-voltage anode-free Li metal batteries. Through a host of advanced characterization techniques, we find that ion cluster sizes decrease with an increasing number of solvents (Fig. 1d). This is attributed to higher solvation entropies driving the thermodynamic equilibrium to favour Li–solvent interactions and suppress ion clustering. HEEs with smaller ion clusters have improved diffusivity compared with low entropy electrolytes (LEEs), which mitigates concentration gradients during high-rate cycling and allows for denser and more uniform deposition morphologies (Fig. 1e). Lastly, we demonstrate the generality of the HEE concept by applying it to fluorinated ether electrolytes and carbonate-based LHCEs. We propose that increasing molecular diversity to modulate the solvation entropy and tune the mesoscopic solvation structure can be a design strategy to improve the ionic conductivity of advanced weakly solvating electrolytes.

Electrolyte design and electrochemical performance

To investigate the effect of entropy on solvation structure, ionic conductivity and battery performance, we systematically change solvation entropy while maintaining similar enthalpic interactions. A route to increasing solvation entropy is increasing the molecular diversity, analogous to increasing the number of elements in high-entropy materials^{35–37}. To minimize differences in enthalpic interaction, however, we select structurally similar solvent compounds with comparable interactions with Li^+ and design three electrolytes with different number of solvents. EL2 (1 M LiFSI in DME-TTE), which

consists of dimethoxyethane (DME) as the solvent and 1,1,2,2-tetrafluoroethyl-2,2,3,3-tetrafluoropropyl ether (TTE) as the co-solvent (Fig. 2a,b and Supplementary Table 3), is an LHCE inspired by refs. 9,28. In LHCEs, the solvent solvates and dissociates ions, whereas the diluent is essentially non-solvating, playing a role to reduce the viscosity and improve the transport properties of the electrolyte while retaining the anion-rich solvation structures of high concentration electrolytes^{31,7}. DME and TTE, together with lithium bis(fluorosulfonyl)imide (LiFSI) salt, was reported to be one of the best solvent mixtures through systematic studies^{16,26}, and showcases one of the best performances for lithium metal batteries^{9,28}. EL4 (1 M LiFSI DME-DEE-DEGDME-TTE) uses three solvents and a co-solvent; diethoxyethane (DEE), diethylene glycol dimethyl ether (DEGDME) and DME are used as solvents, with TTE as the co-solvent. DEE and DEGDME are both glymes that are structurally similar to DME, with DEE containing two ethyl groups in place of methyl groups and DEGDME containing an additional glyme functional group (Fig. 2a and Supplementary Table 3). EL5 (1 M LiFSI DME-DEE-DEGDME-TTE-BTFE), compared with EL4, has an additional fluorinated ether co-solvent, bis(2,2,2-trifluoroethyl) ether (BTFE), which mimics TTE in diluting the electrolyte (Fig. 2b). All electrolytes contain 10% v/v of solvent and 90% v/v of co-solvent (Supplementary Table 3), a ratio designed to be close to salt saturation to eliminate free solvents. By deploying chemically similar compounds without changing the solvent to co-solvent ratio, we expect the nature of intermolecular interactions between solvents, Li^+ and anions to be similar across all electrolytes—which we experimentally confirm later in the discussion—while modulating the solvation entropy.

Figure 2c and Supplementary Fig. 4 show the ionic conductivities of the three electrolytes. EL5 exhibits a remarkable, twofold increase in conductivity compared with EL2. This result is particularly interesting as the viscosities of the electrolytes do not differ appreciably (Supplementary Fig. 5). Figure 2d shows the impedance spectra of Li||Cu cells after Li deposition of 1 mAh cm^{-2} onto the Cu electrodes. This result suggests that the bulk resistance plays a substantial part in the overall impedance in all samples, and the bulk resistance decreases in the order EL2 to EL4 to EL5, further validating the ionic conductivity results (Supplementary Fig. 6). Figure 2e shows the Li||Cu Coulombic efficiency (CE) measurement results (Supplementary Fig. 7 and Supplementary Table 4). At 0.5 mA cm^{-2} , all three electrolytes show excellent CEs around 99.5% and differences in CE across the three electrolytes are negligible. However, at a higher current density of 1 mA cm^{-2} , the CE of EL2 with lower ionic conductivity drops below 98%, whereas EL5 retains 99.4%.

The differences in ionic conductivity and Li||Cu CE translate into the battery cycling performance. Figure 2f–h shows NMC532||Cu anode-free pouch cells with 3.1 mAh cm^{-2} area capacities cycled from 3.0 to 4.4 V at various C-rates (Supplementary Table 5 and Supplementary Fig. 8). At 0.2C charging and 0.5C discharging rates, which are in the range of regularly reported conditions, cyclability increases in the order of EL2 to EL4 to EL5, where EL5 shows anode-free cycling of 110 cycles at 70% capacity retention (Fig. 2f). This effect is magnified at increased rates of 1C charging and 1.5C discharging, where EL5 shows the highest initial capacity and cycling stability (Fig. 2g). At the fast rates of 2C charging and 2C discharging, EL2 and EL4 have limited initial capacity that quickly decays, while EL5 can cycle for almost 80 cycles at 70% capacity retention (Fig. 2h). Overpotential seems to be coupled with capacity retention, as EL5 shows the lowest cycling polarization (Fig. 2f–h) and overpotentials (Fig. 2i–k) at all three C-rates. Cycling polarization is defined in this Article as the difference in average voltages of charging and discharging. This coupling between cycling stability and polarization will be explored in depth later in ‘Electroplating morphology and the interphase’.

To verify the effects of each solvent, we conducted cycling and ionic conductivity characterization for all possible LHCEs from combining three solvents and two co-solvents. The results are shown in

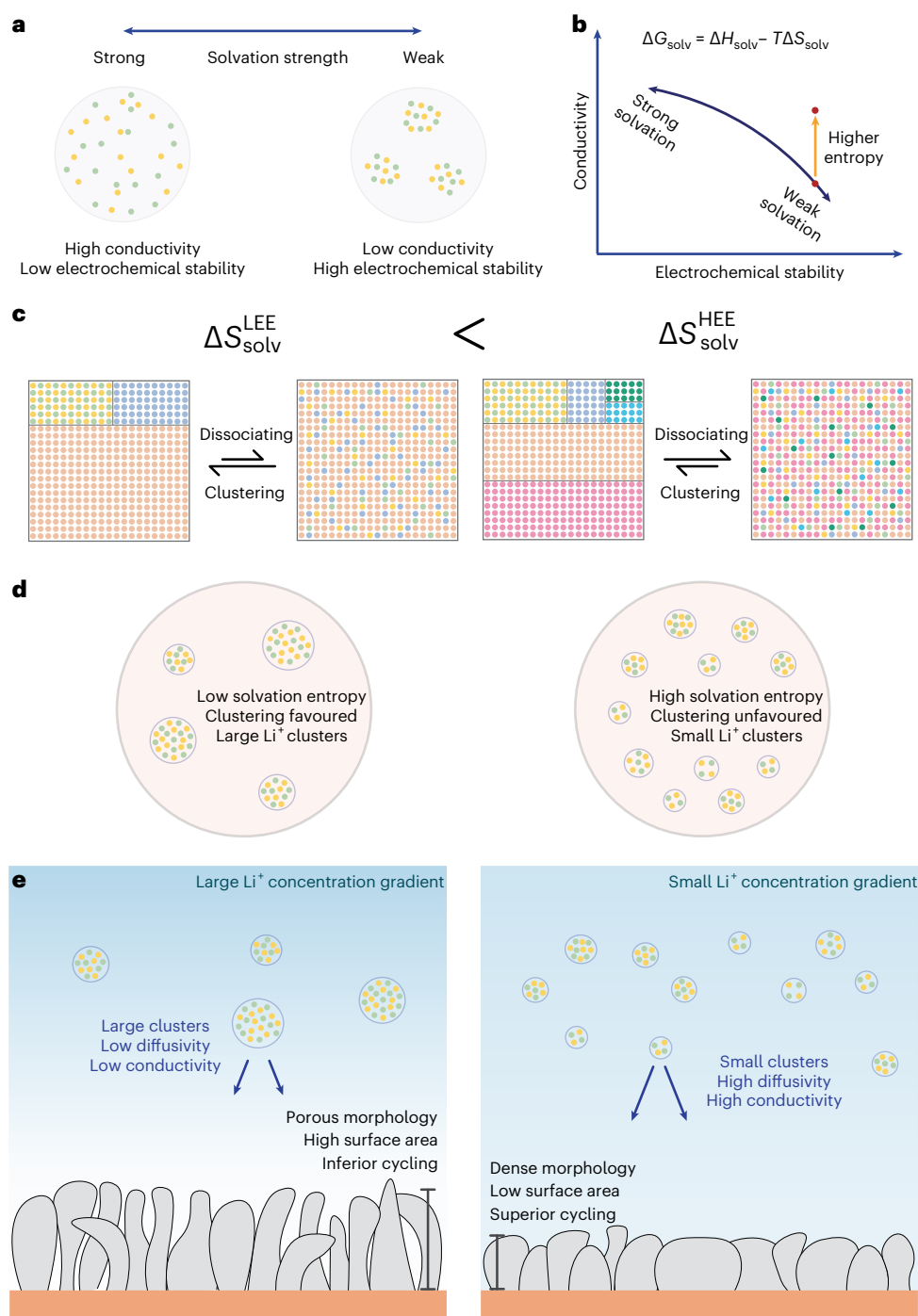


Fig. 1 | Design framework for HEEs. **a**, Schematic illustrating the apparent trade-off between ionic conductivity and electrochemical stability in tuning the solvation strength. Grey circles, individual clusters. **b**, Design concept of increasing solvation entropy to improve ion solvation and enhance ionic conductivity. G_{solv} , H_{solv} and S_{solv} represent solvation free energy, enthalpy and entropy, respectively. **c**, Molecular diversity of HEE increases the solvation entropy, which shifts the thermodynamic equilibrium to promote ion

dissociation and suppress clustering. Large squares represent the electrolyte system. **d**, HEE has smaller ion clusters than LEE. Large circles represent the electrolyte system. **e**, HEE with smaller ion clusters exhibits higher diffusivity and conductivity that leads to a smaller Li^+ concentration gradient and a denser Li deposition morphology during high-rate cycling. The coloured dots in **c** represent individual molecules or ions, whereas only ions are highlighted in **a**, **d** and **e**. Left: LEE depiction; right: HEE depiction (**c**–**e**).

Supplementary Fig. 9. We see that, while different solvents have, to a certain degree, different effects, it is evident that EL5 exhibits performance exceeding that of any single-solvent single-co-solvent mixture (Supplementary Fig. 9). It is important to note, however, that the ionic conductivity improvement from EL2 to EL5, in addition to the entropy effect, has contributions from the BTFE diluent, as it is shown to have better transport properties than TTE. In addition, we also observe

improved oxidative stability for electrolytes with increased number of solvents (Supplementary Fig. 10). We conjecture that this may be due to the fluorine-rich passivating interphase layer (Supplementary Fig. 11), which leads to reduced cracking of the cathode particles during cycling for the HEE (Supplementary Fig. 12). Improved stability at the cathode may also be a contributing factor to the improved cyclability of the HEE. In addition, our electrolytes possess favourable safety

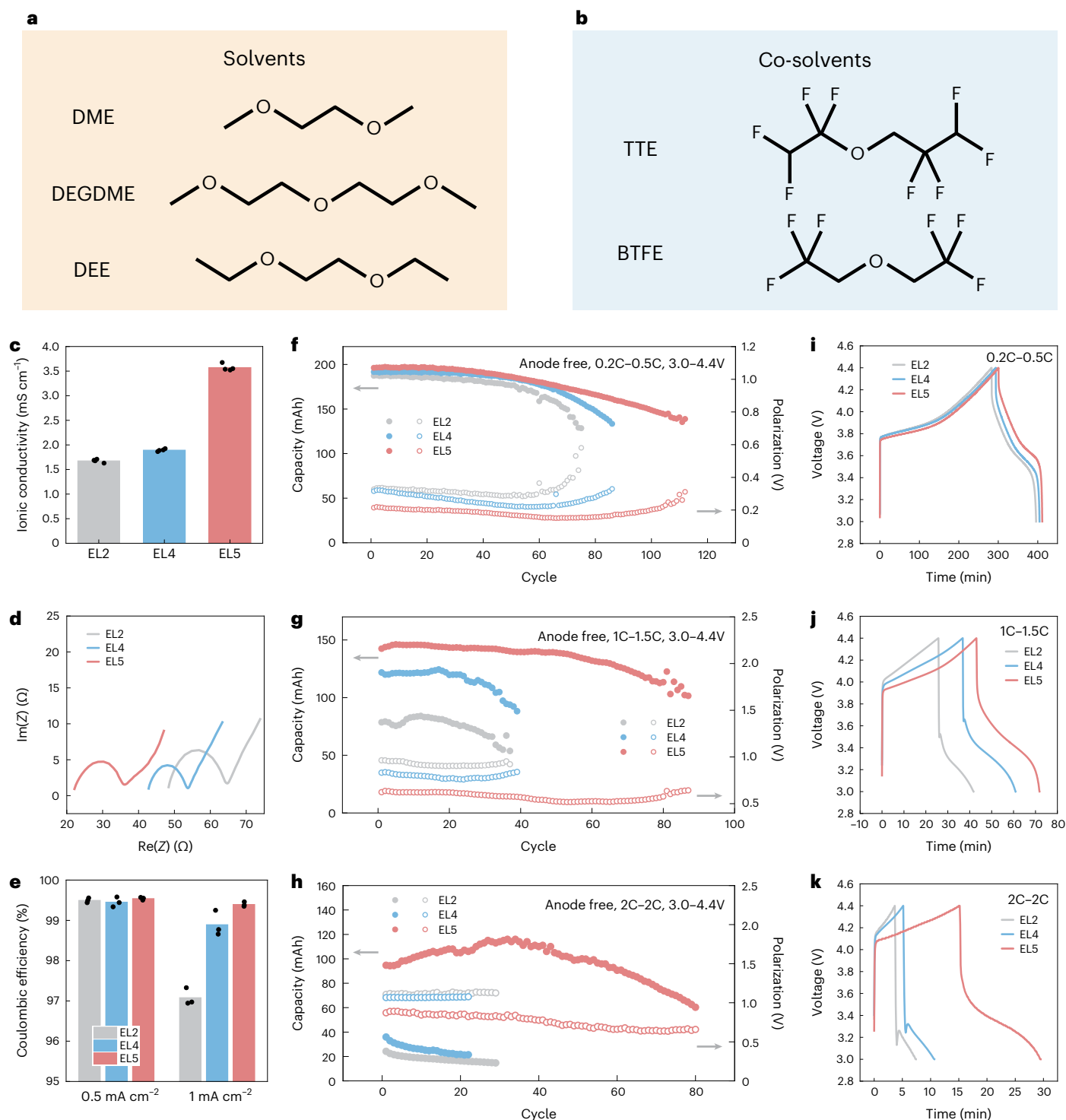


Fig. 2 | Electrochemical performance of HEEs. **a, b**, Chemical structures of the solvents (**a**) and co-solvents (**b**). **c**, Ionic conductivities increase with increasing number of solvents. **d**, Impedance (Z) spectra of Li||Cu coin cells after 1 mA cm^{-2} of Li deposition shows decreased bulk impedance with increasing number of solvents. **e**, Li||Cu Coulombic efficiencies are similar for all electrolytes at 0.5 mA cm^{-2} but show decreased efficiencies for EL2 at 1 mA cm^{-2} . In **c** and **e**, the points signify individual data points and the bar signifies the mean. **f–h**, Anode-

free NMC532-Cu pouch cell cycling at 3.0–4.4 V for different current densities, showing lower polarization and more stable cycling with increased molecular diversity. Charging and discharging C-rates: 0.2C, 0.5C (**f**); 1C, 1.5C (**g**); 2C, 2C (**h**). **i–k**, Voltage profiles of the first cycle during pouch cell cycling, showing lower overpotential with increased molecular diversity. Charging and discharging C-rates: 0.2C, 0.5C (**i**); 1C, 1.5C (**j**); 2C, 2C (**k**).

performance, with much reduced flammability compared with conventional electrolytes (Supplementary Fig. 13 and Supplementary Videos 1–4). Overall, we discover that EL5 with increased molecular diversity has an improved ionic conductivity that correlates with

superior full cell cycling and Li–Cu CE, particularly at higher current densities, and this improvement is unattainable with low molecular diversity. We further validate that these findings hold true to other electrolyte systems in the final section of this study.

Microscopic and mesoscopic solvation structure

We observed greatly improved ionic conductivity for EL5 compared with EL2. To gain molecular-level insights into the differences in conductivity, we investigate the microscopic (ångstrom length scales) and mesoscopic solvation structures (nanometre length scales) through large-scale molecular dynamics (MD) simulations (Supplementary Fig. 14). First, we analyse the microscopic Li coordination environment, where Fig. 3a–c shows the cumulative distribution functions around the Li⁺ for the three electrolytes. It is evident that all three electrolytes have anion-rich solvation structures, containing approximately three anions and one solvent molecules in the first solvation shell. It can be noticed that the co-solvents (TTE and BTFE) do not populate the first solvation shell and lie beyond 4 Å from Li⁺, which is in agreement with previous reports (Supplementary Fig. 15)^{9,16,33}. These results are further corroborated by Raman spectroscopy (Supplementary Fig. 16) and relative solvation enthalpies estimated using potentiometric measurements (Fig. 3d)^{40,41}. Raman spectroscopy confirms that the local solvation structures are similarly anion rich for all three electrolytes, while solvation enthalpies, when compared with a reference electrolyte of 1 M LiFSI in DME, have relatively small differences across the three electrolytes. It can be summarized that the enthalpic interactions between the Li⁺ and the species in the first solvation shell are similar across all electrolytes, and their first solvation structures are all anion rich. As the species in the solvation structure are preferentially decomposed at the anode interface⁴⁰, this leads to the anion-derived solid-electrolyte interphases (SEIs) found in all samples, which will be discussed further in the next section.

Although the microscopic solvation structures are not appreciably different across the three electrolytes, clear differences in mesoscopic structures at the nanometre scale can be observed. Clustering of Li⁺ and anions has been previously reported^{16,33,34} but quantitative analyses of the extent of clustering and the impact on ion transport have been lacking. We performed statistical analyses on the Li⁺ and anion clusters where a large-scale MD simulation was critical to ensuring accurate and statistically significant results. Figure 3e shows the average Li⁺ cluster sizes of the three electrolyte systems at 300 and 350 K, where cluster size is the number of Li⁺ in a discrete cluster (see Methods for the detailed definition). The average cluster size decreases with increased solvent diversity for both temperatures. The simulated results are further confirmed through synchrotron-based X-ray scattering characterization (Fig. 3g and Supplementary Fig. 17). X-ray scattering probes the structures of amorphous materials, analogous to X-ray diffraction for crystalline counterparts, and provides unique insights into the mesoscopic solvation structure such as clusters and networks⁴². Wide-angle X-ray scattering (WAXS) results show that, for scattering vector (*Q*) values of 0.4–1.0 (corresponding to 1.56 and 0.62 nm, respectively), we see that scattering decreases from EL2 to EL5 (Supplementary Fig. 18). This result shows that there is a higher population of larger clusters around 1 nm in diameter in EL2 compared with EL5. This result is further corroborated by other reports on scattering experiments for ion clusters in high-concentration aqueous electrolyte and diluted solvate ionic liquids, where similar *Q* ranges are attributed to the formation of clusters^{42–44}.

Clustering can be an important factor to ionic conductivity. The Stokes–Einstein relation

$$D = \frac{k_B T}{6\pi\eta R} \quad (1)$$

where k_B is the Boltzmann constant, T is temperature, η is viscosity and R is hydrodynamic radius, can serve as a model to aid our understanding of the impact of clustering. The diffusion coefficient (D) is inversely proportional to the hydrodynamic radius, which is directly related to cluster size; increase in cluster size leads to a larger hydrodynamic radius and decreased the diffusivity of ions^{45,46}.

This relationship is verified by diffusion-ordered spectroscopy nuclear magnetic resonance (DOSY-NMR), which can experimentally estimate the diffusion coefficient of Li⁺ (Supplementary Figs. 19 and 20 and Supplementary Table 6). We see in Fig. 3f that Li⁺ diffusion coefficients increase in the order EL2 to EL4 to EL5. Because the viscosities of the three electrolytes do not show appreciable differences (Supplementary Fig. 5), the viscosity effect can be ruled out and thus uncovers the clustering effects. It is possible to reason that the hydrodynamic radii decrease in the order of EL2 to EL4 to EL5, which is consistent with the MD simulation and X-ray scattering results. The Nernst–Einstein relation

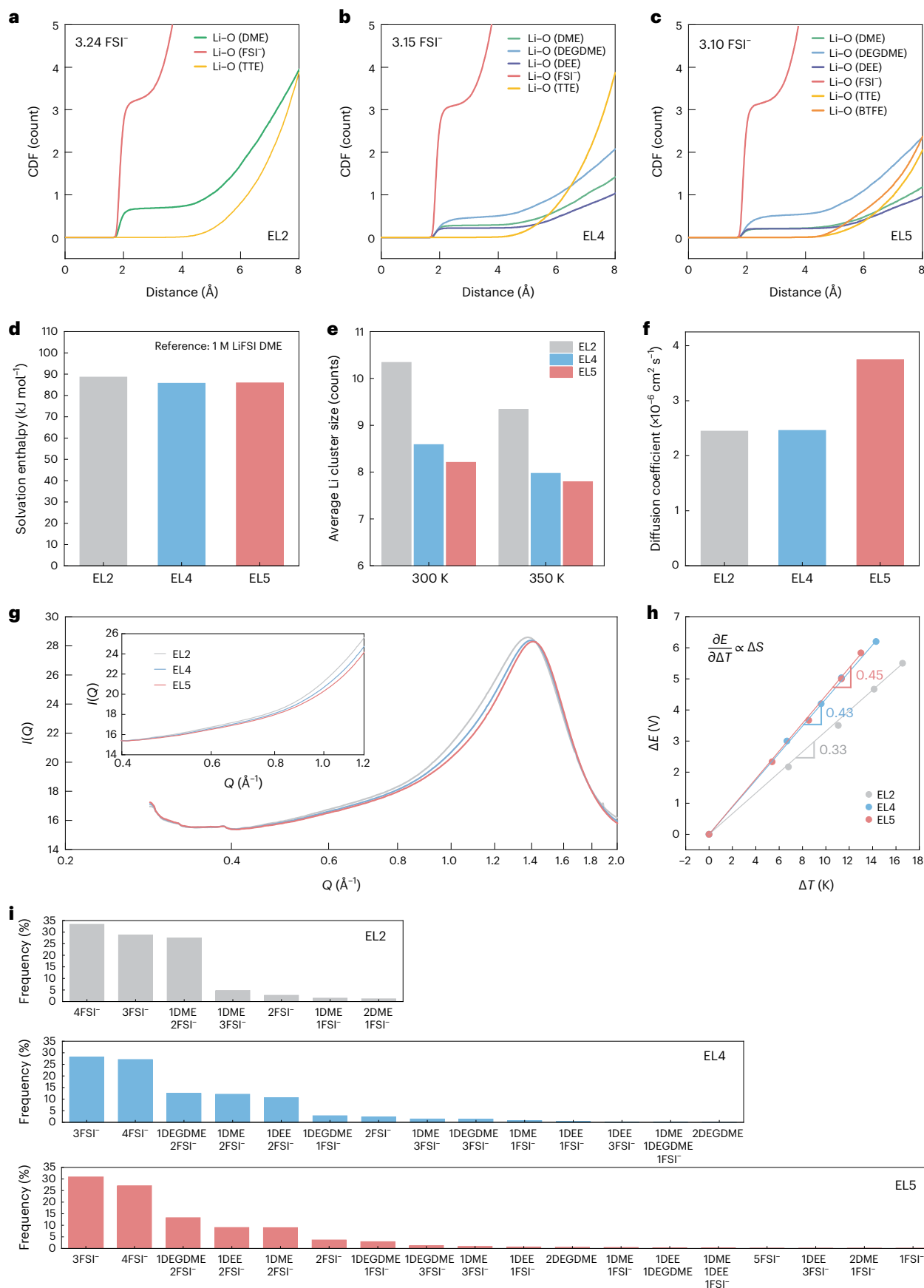
$$\Lambda = \sum \frac{F^2}{RT} (vz^2 D) \quad (2)$$

where Λ is molar conductivity, F is the Faraday constant, R is the gas constant, T is temperature, v is the number of cations or anions and z is charge, can serve as a model to help understand the relationship between diffusivity and conductivity. Although the equation should be taken with caution as some of the assumptions may deviate at practical concentrations of 1 M, it captures the proportionality between conductivity and diffusion coefficient, which is in agreement with our results (Figs. 2c and 3f). In addition to the diffusivity effect on conductivity, larger cluster size will lead to smaller number of clusters, further decreasing the conductivity.

The differences in clustering behaviour that lead to disparate diffusivities and conductivities are attributed to entropic contributions. Solvation entropies, estimated through temperature coefficients of non-isothermal cells⁴¹, show that EL5 has the highest solvation entropy (Fig. 3h). In addition, Fig. 3i shows the make-up of the first solvation shell of the three electrolytes, where it is evident that EL5 with the highest number of solvents has the largest number of possible solvation configurations. We believe that the high entropy of EL5 drives the reduction in clustering and the improvement in ionic conductivity. Electrolyte solvation can be modelled as a product of the thermodynamic equilibrium between dissociating and clustering, balanced by entropic and enthalpic driving forces, as can be stated in the relationship $\Delta G = \Delta H - T\Delta S$ (ref. 47). In most liquid electrolytes, enthalpic forces favour clustering while entropy favours dissociation, and the equilibrium will shift depending on the relative magnitudes (Fig. 1a). This is evidenced by salt solubility increasing with temperature⁴⁸. Because the effect of entropy is magnified at high temperature relative to the enthalpic effect, it is evident that entropic forces drive ion dissolution. Conversely, clustering is entropically unfavourable

Fig. 3 | Microscopic and mesoscopic solvation structures. a–c, Cumulative distribution functions (CDFs) of the electrolytes, EL2 (a), EL4 (b) and EL5 (c), showing anion-rich primary solvation structures. Number of FSI[−] ions in the first solvation shell are indicated in the top-left corner. d, Solvation enthalpy characterized through potentiometric methods shows similar values across the electrolytes. e, The average Li⁺ cluster size obtained with MD simulations decreases with an increasing number of solvents at both 300 K and 350 K. f, Diffusion coefficients measured with DOSY-NMR show the inverse trend of

the cluster sizes. g, WAXS shows decreased clustering with increased molecular diversity. h, Temperature coefficients, signified by the slopes of the lines, show that EL5 has the highest solvation entropy. Points represent the individual measurements, and the slope of the line of best fit correlates to the entropy of solvation, where E is cell voltage. i, Distribution of first solvation structures obtained by MD simulations shows that EL5 has access to the largest number of configurations.



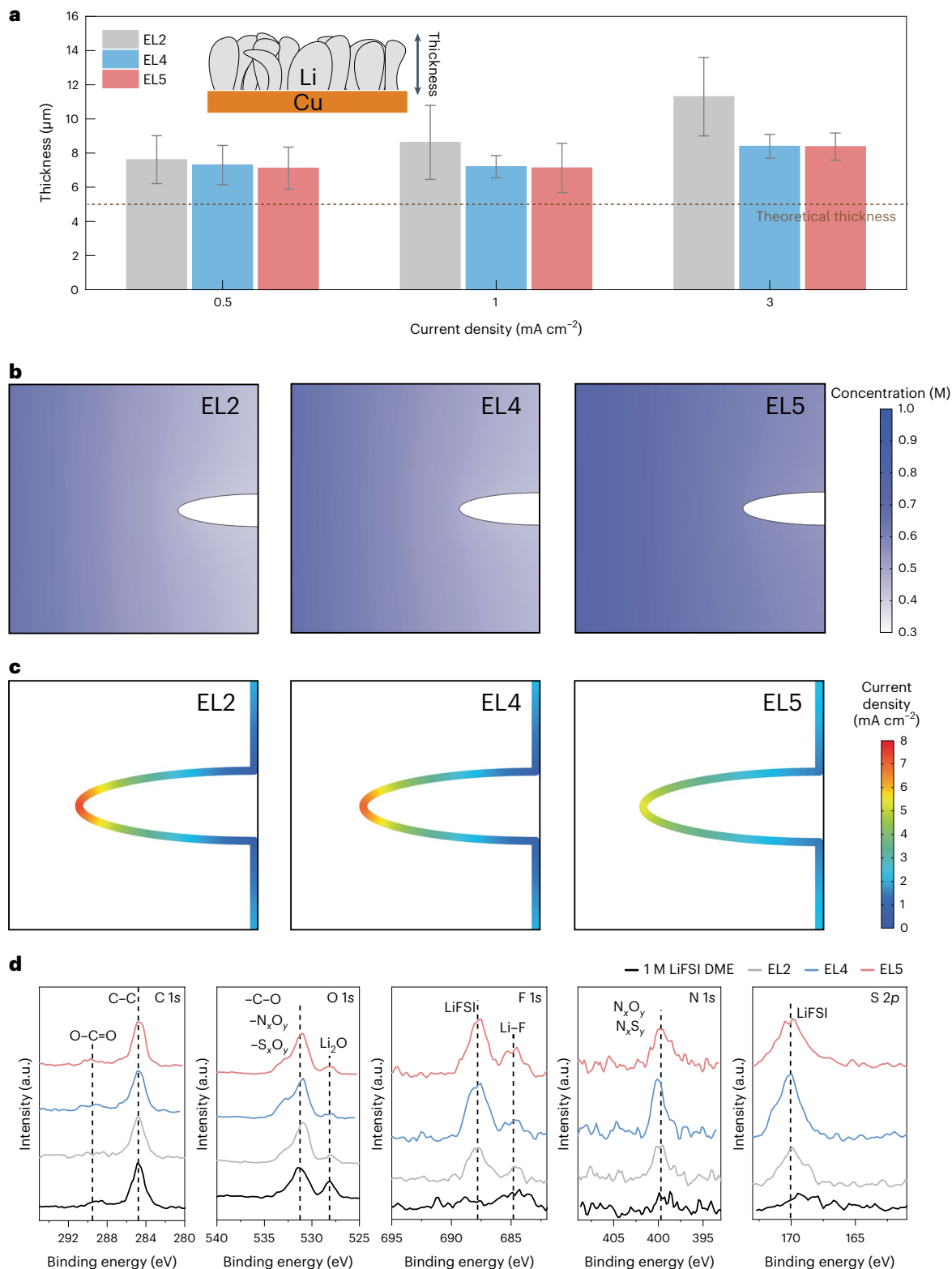


Fig. 4 | Electroplating morphology and the interphase. **a**, Electrodeposition thickness measured by SEM characterization, showing that EL2 has increased thicknesses at high current densities. Error bars, s.d. **b**, Li⁺ concentration gradients in the electrolyte at 3 mA cm⁻², showing that deposition thickness is correlated with concentration gradient build-up at 120 s when steady state is

reached **c**, The local current density profile along the interface of a Li particle shows that electrolytes with large Li⁺ concentration gradients develop large heterogeneities in local current densities at 120 s. **d**, XPS analysis, with peak positions indicated as dotted vertical lines, shows that the three LHCEs have anion-derived SEIs.

and is driven by enthalpy, as evidenced by increased clustering at low temperatures.^{49,50} This general trend applies to our electrolytes, where we observe reduced clustering at 350 relative to 300 K (Fig. 3e). It can be reasoned that HEEs with large solvation entropies will lead to a better dissociated electrolyte with smaller ion clusters with higher mobilities (Fig. 1).

Electroplating morphology and the interphase

We observed that smaller Li cluster formation driven by entropy could improve diffusivity and ionic conductivity. To investigate the relationship between the improved ionic conductivity and high-rate cycling performance, we explore the Li deposition morphology. It is an important determinant of cycling stability as larger deposits reduce the surface area and the Li inventory loss due to SEI formation⁵¹. Scanning electron microscopy (SEM) from the top view shows that all of the electrolytes have large particles of smooth low surface area Li deposits (Supplementary Figs. 21–23). The cross-section view, however, reveals that the Li deposition thicknesses are different (Fig. 4a, Supplementary Fig. 24–26 and Supplementary Table 7) and can be correlated with the cycling stability (Fig. 2). At a low current density of 0.5 mA cm⁻², the differences in thickness are minimal. However, as the current density increases to 1 and 3 mA cm⁻², EL2 with a lower ionic conductivity shows an increase in deposition thickness whereas EL5 retains a dense morphology with a low surface area, which can lead to reduced SEI formation and superior cyclability.

Multiphysics modelling was conducted to investigate the root cause of the discrepancies in Li deposition morphologies at high current densities. Using the electrolytes' physical parameters such as ionic conductivity and the cell parameters such as cathode loading, we simulated the voltage and concentration profiles at different current densities (Fig. 4b and Supplementary Figs. 27 and 28). Figure 4b shows that EL2 forms sharp concentration gradients and Li⁺ depletion at the interface at a plating current density of 3 mA cm⁻², whereas EL5 has a much milder gradient, a phenomenon directly linked to the ionic conductivities and transport properties of the electrolytes. Concentration gradients promote highly heterogeneous current density distributions (Fig. 4c), where current hot-spots at the tip can lead to filamentary and porous deposition morphologies⁵². The relationship between concentration gradient and local current density is illustrated in the extended Butler–Volmer equation (where j signifies the current density, j_0 is the exchange current density, C_{Li} is the local Li concentration at the electrode–electrolyte interface, C_{Li}^* is the reference Li concentration in electrolytes, α_c and α_a are the cathodic and anodic charge-transfer coefficients, z is the number of electrons and η is the overpotential).

$$j = j_0 \left(\frac{C_{Li}}{C_{Li}^*} \right)^{\alpha_a} \left\{ \exp \left[\frac{\alpha_a z F \eta}{RT} \right] - \exp \left[-\frac{\alpha_c z F \eta}{RT} \right] \right\}. \quad (3)$$

Although large concentration gradients are formed at 3 mA cm⁻², we believe that none of the electrolytes reach the Sand's time limit, where the Li⁺ is completely depleted at the Li–electrolyte interface. We do not observe dendritic or mossy lithium (Supplementary Fig. 23), characteristic of such growth modes⁵³, and our Multiphysics simulations show that there remains a finite concentration for all electrolytes (Fig. 4c). Nonetheless, concentration gradients are key factors in shaping the Li deposition morphologies and the cycling stability at high rates.

In addition to the electrolyte transport properties, another factor critical to the battery performance is the SEI. For example, anion-derived inorganic-rich SEIs have been correlated with superior cycling stability^{8,40,54}. We performed X-ray photoelectron spectroscopy (XPS) on the SEIs of the three electrolytes, along with a well-studied reference electrolyte (1 M LiFSI DME^{8,12,21,40}) to investigate the chemical composition of the interphases (Fig. 4d). Compared with 1 M LiFSI

DME, all LHCEs show substantial content of LiFSI salt decomposition products in the SEI, particularly evident in the F 1s, N 1s and S 2p spectra⁵⁵. However, across the three electrolytes, the differences are not pronounced, and clear trends that correlate with the morphologies or electrochemical performance are not present. In particular, differences in the elemental compositions of the SEIs of the three electrolytes are statistically insignificant (Supplementary Fig. 29). In fact, similarity in the SEIs of the three electrolytes is not surprising, considering the similar primary solvation structures of the electrolytes (Fig. 3a–c). The Li⁺ solvation structure is believed to dictate the decomposition products, as components within the solvation structure are more prone to reduction at the Li interface^{40,56}.

Extension to broader electrolyte systems

Molecular diversity as a means to modulate the mesoscopic solvation structure and electrochemical properties can be a powerful and versatile design strategy for high-performance electrolytes. To support its generality, we extended the idea to fluorinated ether electrolytes and carbonate-based LHCEs (Fig. 5a,b). A series of fluorinated diethoxyethane (FDEE) solvents have been developed recently by our group, which were deployed in electrolytes with state-of-the-art electrochemical performance for lithium metal batteries¹⁰. We applied the high-entropy concept to FDEEs to further improve the electrochemical performance, especially their transport properties. Our high-entropy FDEE electrolyte is an equivolume mixture of the four solvents F3DEE–F6DEE (F3–6DEE), mixed with 1 M of LiFSI salt. We compare the electrolyte with F5DEE solvent mixed with the same salt, as the solvent displayed the most stable cycling among the four solvents¹⁰, and consequently the averaged performance of the electrolytes containing F3–6DEE would be inferior to that using F5DEE. Reassuringly, the high-entropy FDEE electrolyte (F3–6DEE) displays superior ionic conductivity and high-rate cycling stability (Fig. 5c–g). The ionic conductivity is improved by ~50% by diversifying the solvents (Fig. 5c and Supplementary Fig. 30). This is surprising in that F3DEE, the solvent with the highest conductivity among the FDEEs, has only a ~20% higher conductivity than F5DEE¹⁰. The remarkable improvement is correlated with molecular diversity. The CEs of Li||Cu cells are also slightly improved, with F3–6DEE having a CE of 99.6% (Fig. 5d and Supplementary Fig. 31). Anode-free pouch cell cycling of F3–6DEE shows notable improvement at higher rates of 1C–1.5C and 2C–2C compared with its single-solvent counterpart. As FDEEs are weakly solvating solvents owing to the electron-withdrawing effects of fluorination, a large fraction of Li ions exist as clusters¹⁰. We expect the increased solvation entropy in F3–6DEE electrolyte to mitigate clustering and improve the diffusivity and conductivity of Li⁺, improving the ionic conductivity and cyclability at high rates.

As another example of HEEs, we developed high-entropy carbonate LHCEs. Dimethyl carbonate (DMC), ethyl methyl carbonate (EMC) and diethyl carbonate (DEC) were used as solvents (Fig. 5b), being mixed with TTE and BTFE co-solvents. The solvents are linear carbonates that differ by the length of the hydrocarbon chain and exhibit close physicochemical properties⁵⁷. EMC-TTE was selected as EL2, as EMC has properties that are intermediate between those of DEC and DMC⁵⁷. Figure 5h,i and Supplementary Figs. 32 and 33 illustrate that EL5c has the highest ionic conductivity and Li||Cu CE at higher current densities, consistent with the trend for ether-based LHCEs. In addition, the NMC532||Cu anode-free pouch cell cyclability increases in the order of EL2c to EL4c to EL5c, confirming the trend that increasing the solvent diversity can lead to improved cycle life (Fig. 5j and Supplementary Fig. 34). We demonstrate that judiciously designed HEEs have demonstrated improved performance, but it is important to note that individual components must be chosen carefully; using components with unfavourable properties can be detrimental to the performance of the HEE.

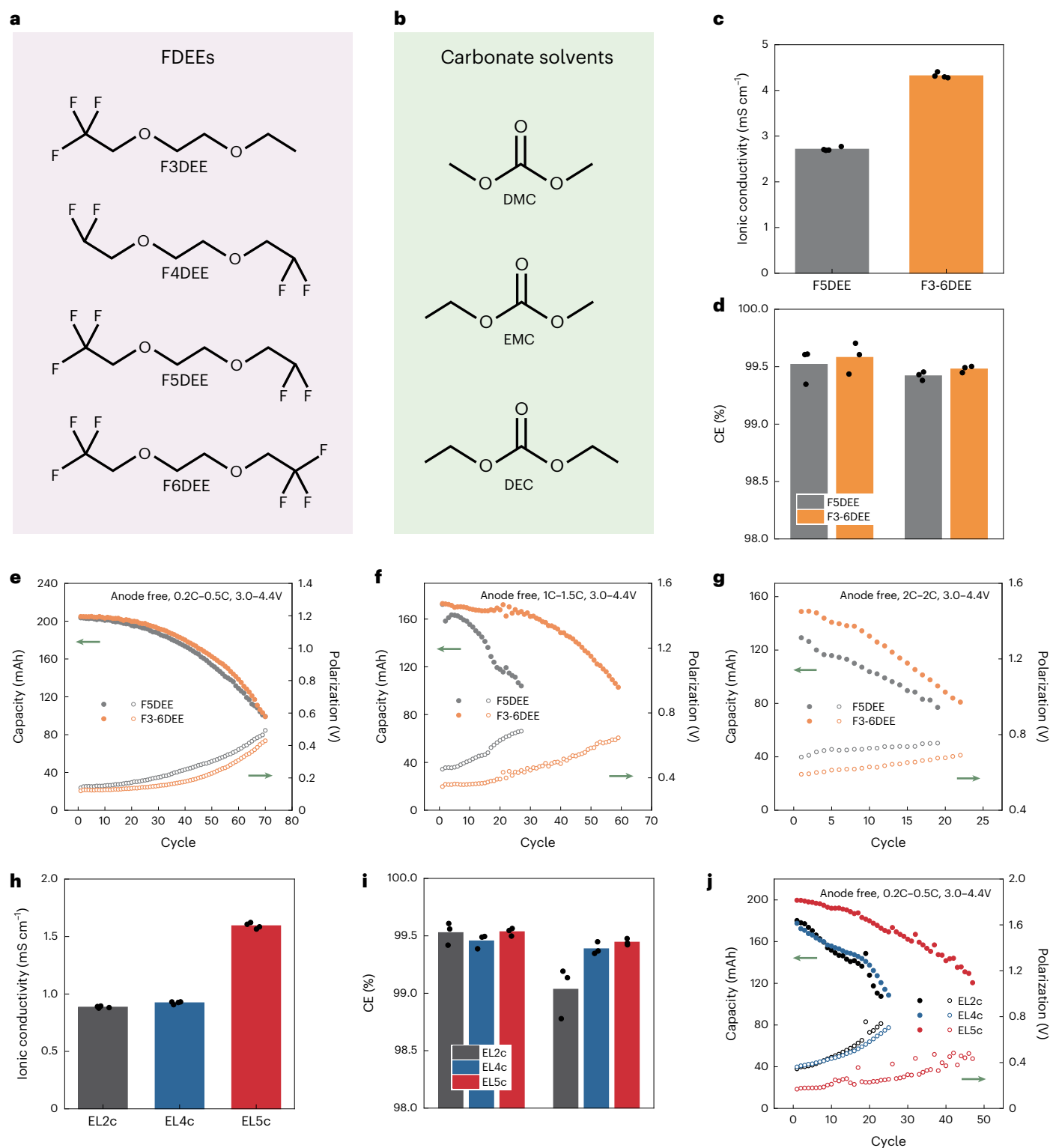


Fig. 5 | Electrochemical performance of broader HEE systems. **a, b**, Chemical structure of solvents used in high-entropy FDEEs (**a**) and high-entropy carbonate LHCEs (**b**). **c**, The ionic conductivity of F3-6DEE shows a ~50% increase from F5DEE. **d**, Li||Cu CE are slightly improved for F3-6DEEs. **e–g**, Anode-free NMC532-Cu pouch cell cycling at 3.0–4.4 V for different current densities, showing lower polarization and more stable cycling for F3-6DEE. Charging and discharging rates: 0.2C, 0.5C (**e**); 1C, 1.5C (**f**); 2C, 2C (**g**). **h**, Ionic conductivities

increase with increasing number of solvents. **i**, Li||Cu CE are similar for EL2-5c at 0.5 mA cm^{-2} but show decreased efficiencies for EL2c at 1 mA cm^{-2} . **j**, Anode-free NMC532-Cu pouch cell cycling at 3.0–4.4 V for different current densities, showing lower polarization and more stable cycling with increased number of solvents. Charging and discharging rates: 0.2C, 0.5C. Points are individual measurements and bar represent the mean (**c, d, h, i**).

Conclusions

Here, we show that molecular diversity as a design strategy can be applied widely to many electrolyte systems and provides a vast unexplored design space of HEEs. In particular, the strategy can be utilized to modulate the mesoscopic solvation structures in weakly solvating electrolytes where extensive amounts of ion clustering are present, which has been demonstrated through X-ray scattering and simulations in this work. Electrolytes with smaller-sized clusters are shown to improve transport properties and fast-charging capabilities, which we confirmed through DOSY-NMR and electrochemical characterizations. We envision that this work can spur efforts to develop HEEs that can push lithium metal batteries closer to practical applications and to broadly develop high-entropy solutions with superior properties for various applications.

Methods

Electrolyte preparation

All electrolytes were prepared and handled in an argon-filled glovebox with O₂ concentration <0.2 ppm and H₂O concentration <0.01 ppm. All electrolyte materials were used as received after molecular sieving to remove trace amounts of water. LiFSI (Fluolyte) was used as the salt. DME (Sigma-Aldrich), DEGDME (Sigma-Aldrich), DEE (Acros), DMC (Sigma-Aldrich), EMC (Sigma-Aldrich), DEC (Sigma-Aldrich), TTE (SynQuest) and BTFE (SynQuest) were used as solvents. The fluorinated DEE (FDEE) solvents were synthesized in the laboratory using methods described ref. 10. The electrolytes were filtered before use to eliminate any potentially remaining solid particles.

Electrochemical performance testing

All pouch cells were commercial single-crystal NMC532||Cu dry pouch cells purchased from Li-Fun Technology, with -3.1 mAh cm⁻² of cathode loading and cell capacity of -200 mAh, then electrolytes were pipetted into the cells in an argon-filled glovebox. Pouch cells were cycled using Biologic VMP3, first cycled with two formation cycles at C/10. Subsequent cycles were constant-current cycles at different C-rates with voltage ranges of 3.0–4.4 V. All pouch cells were pressurized using C-clamps and polyacrylic plates. The 2032-type coin cells were assembled in the glovebox using Celgard 2325 separators and NMC532 electrodes purchased from MTI. Coin cells were used for impedance, cycling, linear sweep voltammetry, Coulombic efficiency and electrode characterizations. Coin cell cycling was conducted using Land Instruments cyclers. Electrochemical impedance spectroscopy measurements were taken over the frequency range from 1 MHz to 100 mHz. Linear sweep voltammetry tests were carried out over a voltage range of 3–6 V in Li||Al cells. For Li||Cu half-cell CE tests, initially 5 mAh cm⁻² of Li metal was deposited on Cu and stripped (formation cycle). Then, 5 mAh cm⁻² of Li metal was deposited again, to act as a Li reservoir. Then, Li was repeatedly stripped and plated 1 mAh cm⁻² for nine cycles. The remaining Li on Cu was then stripped, and the average CE was calculated by dividing the total stripping capacity by the total plating capacity after the formation cycle. LiNiMnCoO₂ (NMC)||Cu full cells were first cycled with two formation cycles at C/10. Subsequent cycles were constant-current cycles at different C-rates with voltage ranges of 3.0–4.4 V. For ionic conductivity measurements, a Swagelok cell was used with no separators and electrochemical impedance spectroscopy was used to measure the bulk resistance, which was then converted into conductivity using the length and area of the cell.

MD simulations

MD simulations were carried out using the LAMMPS package. The optimized potentials for liquid simulations all-atom force field⁵⁸ with fitted parameters for LiFSI⁵⁹ and the solvent molecules DME, DEGDME, DEE and BTFE³³ was used in this work, where the parameters for TTE were fitted specifically for this work (Supplementary Table 10). Parameter fitting was performed using the density functional theory package Orca⁶⁰, with the 6-31++G(d,p) basis set and long-range corrected

Becke–Lee–Yang–Parr functional. The atomic charges for all species in this work are re-calculated using RESP analysis implemented in the Multiwfn package⁶¹. The EL2 system contains 384 DME molecules, 2,376 TTE molecules and 400 LiFSI molecules. The EL4 system contains 128 DME molecules, 96 DEE molecules, 92 DEGDME molecules, 2,376 TTE molecules and 400 LiFSI molecules. The EL5 system contains 128 DME molecules, 96 DEE molecules, 92 DEGDME molecules, 1,388 TTE molecules, 1,188 BTFE molecules and 400 LiFSI molecules. The systems were initialized randomly using the Packmol package. The systems were then subjected to a simulated annealing equilibration protocol as follows: (1) energy minimization at temperature $T = 0$ K, (2) equilibration at $T = 300$ K for 2 ns in a number–pressure–temperature (*NPT*) ensemble, (3) heating up the system to 450 K over 1 ns in an *NPT* ensemble, (3) relaxation at $T = 450$ K over 1 ns in an *NPT* ensemble, (4) cooling down to $T = 300$ K over 1 ns in an *NPT* ensemble and (5) equilibration at $T = 300$ K for 5 ns in an *NPT* ensemble. The production run was subsequently performed at $T = 300$ K over 20 ns in a number–volume–temperature (*NVT*) ensemble. A second round of simulations with the equilibrium temperature $T = 350$ K were performed to study the entropic effects on cluster distribution. All the simulations in this work used a timestep of 1 fs and a pressure of 1 atm. The temperature and pressure were regulated with a Nosé–Hoover thermostat and barostat, with a damping parameter of 0.2 ps and 1 ps, respectively.

The subsequent data analysis was carried out using the last 10 ns of the production run trajectories. The cumulative distribution functions and the first solvation shell coordination numbers were calculated by using the python code MDAnalysis⁶². The time averaging used snapshots taken every 250 ps to minimize temporal correlation effects. Structural analysis of salt ion clusters was carried out with custom code based on the breadth-first search algorithm. Specifically, the program starts with one random unvisited Li⁺ atom as the starting atom (henceforth marked as visited) of a cluster and searches for its neighbouring O atoms. The FSI⁻ anions to which each O atom belongs are henceforth marked as visited and part of the cluster. This primary step is followed by a secondary step, where for every O atom of the marked FSI⁻ ions in the primary step, its unvisited neighbouring Li⁺ ions are henceforth marked as visited as part of the cluster. These two steps are performed recursively to determine all the Li⁺ and FSI⁻ ions belonging to one common cluster. This search process is repeated for the whole system to determine the statistics of clusters present in the system. The criterion for neighbouring atoms is that their interatomic distance be less than 2.5 Å.

COMSOL Multiphysics simulations

All the multiphysics simulations on lithium electrodeposition were performed using COMSOL Multiphysics software. The electric current (i_i) in the electrolyte is governed by the diffusion and migration of Li ions and can be described using the Nernst–Planck equation:

$$i_i = (-K_i \nabla \phi_i) + \frac{2K_i RT}{F} \left(1 + \frac{\partial \ln f}{\partial \ln C_{Li}} \right) (1 - t_+) \nabla \ln C_{Li} \quad (4)$$

where K_i is the ionic conductivity of the electrolyte, ϕ_i is the electrolyte potential, C_{Li} is the concentration of Li⁺ in the electrolyte, R is the gas constant, T is temperature, F is the Faraday constant, t_+ is the transference number of Li⁺ and f is the mean molar activity coefficient of the electrolyte. The Butler–Volmer equation was used to describe the relationship between the electrodeposition rate and the electrodeposition overpotential:

$$j = j_0 \left(\frac{C_{Li}}{C_{Li}^*} \right)^{\alpha_a} \left\{ \exp \left[\frac{\alpha_a z F \eta}{RT} \right] - \exp \left[-\frac{\alpha_c z F \eta}{RT} \right] \right\}, \quad (5)$$

where j signifies the current density, j_0 is the exchange current density and C_{Li}^* is the reference Li concentration in electrolytes. α_c and α_a are

the cathodic and anodic charge-transfer coefficients and z is the number of electrons. The overpotential for lithium electrodeposition is defined as $\eta = \phi_s - \phi_l$, where ϕ_s is the electrode potential.

The mass transport of Li^+ in the electrolyte is defined as

$$\frac{\partial C_1}{\partial t} + \nabla \cdot J_1 = 0, \quad (6)$$

$$J_1 = -D_1 \nabla C_1 + \frac{i_1 t_+}{F} \quad (7)$$

where J_1 represents Li^+ flux in the electrolyte, t is time and D_1 stands for the Li^+ diffusivity in electrolytes.

The physical parameters of electrolytes (EL2, EL4 and EL5) and electrodes (NMC and Li metal) in the numerical model are set to be consistent with the experiments (Table 1 and Supplementary Table 11). The anode-free cell configuration is used in the numerical model, in which the thicknesses of the NMC cathode and separator are set to be 70 and 25 μm .

Electrode and interphase characterization

SEM images were taken using an FEI Magellan 400 XHR. The 2032-type Li||Cu coin cells were assembled using a Celgard 2325 separator with respective electrolytes. Li was plated 1 mAh cm^{-2} onto a Cu current collector using various current densities. Then, the coin cell was disassembled in a glovebox and the electrode was extracted then washed in DME to remove any excess Li salt. For cross-section imaging, the electrodes were torn and mounted onto the SEM holder for imaging. The images were used to measure the cross-section thicknesses (see Supplementary Fig. 7 for raw data). The error bars shown in Fig. 4a represent standard deviations. XPS signals were collected on a PHI VersaProbe 1 scanning XPS microprobe with an Al K_α source. Li was deposited 1 mAh cm^{-2} onto Cu current collectors at 0.5 mA cm^{-2} current density, and SEI was characterized without sputtering. For cathode characterizations, NMC532-Cu coin cells were cycled for 50 cycles at 1 mA cm^{-2} current density then rinsed with DME before characterization.

Electrolyte characterization

Solvation entropy measurements were done using a potentiometric method developed previously in our group⁴⁰, using a non-isothermal cell with Li metal as electrodes. A temperature gradient was progressively developed, and the voltage response was recorded. The slope of voltage versus temperature gradient, determined with the line of best fit to minimize residuals, was used to estimate the solvation entropy. Solvation energy measurements were done by using a similar method, using a H-cell with Li metal as electrodes and asymmetric electrolytes. An open circuit potential was measured to probe the relative solvation energy. The steady-state viscosity was measured at ambient condition with a TA Instrument ARES-G2 rheometer in parallel plate geometry.

X-ray scattering characterization

Synchrotron small-angle x-ray scattering was conducted in capillary transmission mode at beamline I-5 at the Stanford Synchrotron Radiation Lightsource of SLAC National Accelerator Laboratory, with 15 keV beam energy. The detector is Dectris Pilatus 1M, with a sample to detector distance of 835.685 mm. All measurements were done in ambient air condition. Three spots along each sample capillary holder were collected, with an exposure time of 60 s for each spot and ten repeats for each spot. Two-dimensional scattering data were exported into IgorPro, processed with the Irena and Nika packages and calibrated with the LaB6 standard. The one-dimensional data are normalized with the beamstop value, and background subtraction was done with data collected for the empty quartz capillaries (outer diameter 2 mm, Charles Supper).

Synchrotron wide-angle X-ray scattering was conducted in capillary transmission mode at beamline 11-3 at the Stanford Synchrotron

Radiation Lightsource of SLAC National Accelerator Laboratory, with 12.7 keV beam energy. The detector is Raxyonics 225, 73.242 μm (ref. 2), with a sample to detector distance of 150 mm. All measurements were done in ambient air condition. Seven spots along each sample capillary holder were collected, with an exposure time of 25 s for each spot. Two-dimensional scattering data were exported and processed with the beamline customized software xdart and calibrated with the LaB6 standard. All one-dimensional data were normalized with the intensity value of high Q (5 \AA^{-1}).

DOSY-NMR characterization

In an argon glovebox, electrolyte was injected into a thin-walled NMR tube. Ten percent toluene was added as an internal reference. A co-axial tube containing DMSO- d_6 was inserted into the NMR tube. The caps of the outer and inner tubes were sealed by parafilm to avoid moisture during DOSY-NMR experiment. All DOSY-NMR experiments were performed on a Varian 400 MHz spectrometer at 25 °C. ^7Li -pulsed field gradient (PFG) measurements were performed to determine the diffusion coefficients using the standard *dsteppg3s* pulse sequence. The array of gradient strength was set to 2.908–12.504 G cm^{-1} with 12 linear steps. The recycling delay (*d1*) was 1 s. The high power 90° pulse (*pw90*) was 9 μs . The acquisition time was 4 s. The diffusion delay (Δ) was 0.5 s for EL2 and 0.46 s for EL4 and EL5. The gradient pulse duration (δ) was 9 ms. Apparent diffusion coefficients were calculated by fitting peak integrals to the Stejskal–Tanner equation.

Data availability

All data are available in the main text or the Supplementary Information.

References

- Whittingham, M. S. Electrical energy storage and intercalation chemistry. *Science* **192**, 1126–1127 (1976).
- Lin, D., Liu, Y. & Cui, Y. Reviving the lithium metal anode for high-energy batteries. *Nat. Nanotechnol.* **12**, 194–206 (2017).
- Zhang, J. G., Xu, W., Xiao, J., Cao, X. & Liu, J. Lithium metal anodes with nonaqueous electrolytes. *Chem. Rev.* **120**, 13312–13348 (2020).
- Winter, M., Barnett, B. & Xu, K. Before Li ion batteries. *Chem. Rev.* **118**, 11433–11456 (2018).
- Lin, D. et al. Layered reduced graphene oxide with nanoscale interlayer gaps as a stable host for lithium metal anodes. *Nat. Nanotechnol.* **11**, 626–632 (2016).
- Zhou, L. et al. High areal capacity, long cycle life 4 V ceramic all-solid-state Li ion batteries enabled by chloride solid electrolytes. *Nat. Energy* **7**, 83–93 (2022).
- Fu, C. et al. Universal chemomechanical design rules for solid-ion conductors to prevent dendrite formation in lithium metal batteries. *Nat. Mater.* **19**, 758–766 (2020).
- Cao, X. et al. Monolithic solid–electrolyte interphases formed in fluorinated orthoformate-based electrolytes minimize Li depletion and pulverization. *Nat. Energy* **4**, 796–805 (2019).
- Ren, X. et al. Enabling high-voltage lithium metal batteries under practical conditions. *Joule* **3**, 1662–1676 (2019).
- Yu, Z. et al. Rational solvent molecule tuning for high-performance lithium metal battery electrolytes. *Nat. Energy* <https://doi.org/10.1038/s41560-021-00962-y> (2022).
- Fan, X. et al. All-temperature batteries enabled by fluorinated electrolytes with non-polar solvents. *Nat. Energy* **4**, 882–890 (2019).
- Chen, Y. et al. Steric-effect-tuned ion solvation enabling stable cycling of high-voltage lithium metal battery. *J. Am. Chem. Soc.* <https://doi.org/10.1021/jacs.1c09006> (2021).
- Louli, A. J. et al. Diagnosing and correcting anode-free cell failure via electrolyte and morphological analysis. *Nat. Energy* **5**, 693–702 (2020).

14. Kim, M. S. et al. Suspension electrolyte with modified Li⁺ solvation environment for lithium metal batteries. *Nat. Mater.* <https://doi.org/10.1038/s41563-021-01172-3> (2022).
15. Wang, H. et al. Liquid electrolyte: the nexus of practical lithium metal batteries. *Joule* <https://doi.org/10.1016/j.joule.2021.12.018> (2022).
16. Cao, X. et al. Effects of fluorinated solvents on electrolyte solvation structures and electrode/electrolyte interphases for lithium metal batteries. *Proc. Natl Acad. Sci. USA* **118**, e2020357118 (2021).
17. Chen, S. et al. High-voltage lithium metal batteries enabled by localized high-concentration electrolytes. *Adv. Mater.* **30**, 1706102 (2018).
18. Zheng, J. et al. High-fluorinated electrolytes for Li-S batteries. *Adv. Energy Mater.* **9**, 1803774 (2019).
19. Xue, W. et al. Ultra-high-voltage Ni-rich layered cathodes in practical Li metal batteries enabled by a sulfonamide-based electrolyte. *Nat. Energy* <https://doi.org/10.1038/s41560-021-00792-y> (2021).
20. Holoubek, J. et al. Electrolyte design implications of ion pairing in low-temperature Li metal batteries. *Energy Environ. Sci.* **15**, 1647–1658 (2022).
21. Yu, Z. et al. Molecular design for electrolyte solvents enabling energy-dense and long-cycling lithium metal batteries. *Nat. Energy* **5**, 526–533 (2020).
22. Chen, S. et al. High-efficiency lithium metal batteries with fire-retardant electrolytes. *Joule* **2**, 1548–1558 (2018).
23. Berhaut, C. L. et al. Ionic association analysis of LiTDI, LiFSI and LiPF₆ in EC/DMC for better Li ion battery performances. *RSC Adv.* **9**, 4599–4608 (2019).
24. Lundgren, H., Behm, M. & Lindbergh, G. Electrochemical characterization and temperature dependency of mass-transport properties of LiPF₆ in EC:DEC. *J. Electrochem. Soc.* **162**, A413–A420 (2014).
25. Yamada, Y. et al. Unusual stability of acetonitrile-based superconcentrated electrolytes for fast-charging lithium ion batteries. *J. Am. Chem. Soc.* **136**, 5039–5046 (2014).
26. Ren, X. et al. Role of inner solvation sheath within salt–solvent complexes in tailoring electrode/electrolyte interphases for lithium metal batteries. *Proc. Natl Acad. Sci. USA* **117**, 28603–28613 (2020).
27. Ren, X. et al. Localized high-concentration sulfone electrolytes for high-efficiency lithium metal batteries. *Chem* **4**, 1877–1892 (2018).
28. Niu, C. et al. Balancing interfacial reactions to achieve long cycle life in high-energy lithium metal batteries. *Nat. Energy* **6**, 723–732 (2021).
29. Weber, R. et al. Long cycle life and dendrite-free lithium morphology in anode-free lithium pouch cells enabled by a dual-salt liquid electrolyte. *Nat. Energy* **4**, 683–689 (2019).
30. Genovese, M. et al. Hot formation for improved low temperature cycling of anode-free lithium metal batteries. *J. Electrochem. Soc.* **166**, A3342–A3347 (2019).
31. Louli, A. J. et al. Exploring the impact of mechanical pressure on the performance of anode-free lithium metal cells. *J. Electrochem. Soc.* **166**, A1291–A1299 (2019).
32. Wang, H. et al. Dual-solvent Li-ion solvation enables high-performance Li metal batteries. *Adv. Mater.* **33**, 2008619 (2021).
33. Perez Beltran, S., Cao, X., Zhang, J. G. & Balbuena, P. B. Localized high concentration electrolytes for high voltage lithium metal batteries: correlation between the electrolyte composition and its reductive/oxidative stability. *Chem. Mater.* **32**, 5973–5984 (2020).
34. Liu, H. et al. Ultrahigh coulombic efficiency electrolyte enables Li||SPAN batteries with superior cycling performance. *Mater. Today* **42**, 17–28 (2021).
35. Ye, Y. F., Wang, Q., Lu, J., Liu, C. T. & Yang, Y. High-entropy alloy: challenges and prospects. *Mater. Today* **19**, 349–362 (2016).
36. Lun, Z. et al. Cation-disordered rocksalt-type high-entropy cathodes for Li ion batteries. *Nat. Mater.* **20**, 214–221 (2021).
37. Oses, C., Toher, C. & Curtarolo, S. High-entropy ceramics. *Nat. Rev. Mater.* **5**, 295–309 (2020).
38. Wang, Q. et al. Multi-anionic and -cationic compounds: new high-entropy materials for advanced Li ion batteries. *Energy Environ. Sci.* **12**, 2433–2442 (2019).
39. Zeng, Y. et al. High-entropy mechanism to boost ionic conductivity. *Science* **378**, 1320–1324 (2022).
40. Kim, S. C. et al. Potentiometric measurement to probe solvation energy and its correlation to lithium battery cyclability. *J. Am. Chem. Soc.* **143**, 10301–10308 (2021).
41. Wang, H. et al. Correlating Li ion solvation structures and electrode potential temperature coefficients. *J. Am. Chem. Soc.* <https://doi.org/10.1021/jacs.0c10587> (2021).
42. Qian, K., Winans, R. E. & Li, T. Insights into the nanostructure, solvation, and dynamics of liquid electrolytes through small-angle X-ray scattering. *Adv. Energy Mater.* **11**, 2002821 (2021).
43. Saito, S. et al. Li⁺ local structure in hydrofluoroether diluted Li-glyme solvate ionic liquid. *J. Phys. Chem. B* **120**, 3378–3387 (2016).
44. Zheng, J. et al. Understanding thermodynamic and kinetic contributions in expanding the stability window of aqueous electrolytes. *Chem* **4**, 2872–2882 (2018).
45. Hassan, S. A. Morphology of ion clusters in aqueous electrolytes. *Phys. Rev. E* **77**, 1–5 (2008).
46. Tan, P. et al. Solid-like nano-anion cluster constructs a free lithium-ion-conducting superfluid framework in a water-in-salt electrolyte. *J. Phys. Chem. C* **125**, 11838–11847 (2021).
47. McEldrew, M., Goodwin, Z. A. H., Bi, S., Bazant, M. Z. & Kornyshev, A. A. Theory of ion aggregation and gelation in super-concentrated electrolytes. *J. Chem. Phys.* **152**, 234506 (2020).
48. Xin, N., Sun, Y., He, M., Radke, C. J. & Prausnitz, J. M. Solubilities of six lithium salts in five non-aqueous solvents and in a few of their binary mixtures. *Fluid Phase Equilib.* **461**, 1–7 (2018).
49. McEldrew, M., Goodwin, Z. A. H., Zhao, H., Bazant, M. Z. & Kornyshev, A. A. Correlated ion transport and the gel phase in room temperature ionic liquids. *J. Phys. Chem. B* **125**, 10, 2677–2689 (2021).
50. Gupta, A. & Manthiram, A. Unifying the clustering kinetics of lithium polysulfides with the nucleation behavior of Li₂S in lithium–sulfur batteries. *J. Mater. Chem. A* **9**, 13242–13251 (2021).
51. Fang, C. et al. Pressure-tailored lithium deposition and dissolution in lithium metal batteries. *Nat. Energy* **6**, 987–994 (2021).
52. Xiao, B. J. How lithium dendrites form in liquid batteries. *Science* **366**, 426–428 (2019).
53. Bai, P., Li, J., Brushett, F. R. & Bazant, M. Z. Transition of lithium growth mechanisms in liquid electrolytes. *Energy Environ. Sci.* <https://doi.org/10.1039/C6EE01674J> (2016).
54. Fan, X. et al. Highly fluorinated interphases enable high-voltage Li metal batteries. *Chem* **4**, 174–185 (2018).
55. Oyakhire, S. T., Gong, H., Cui, Y., Bao, Z. & Bent, S. F. An X-ray photoelectron spectroscopy primer for solid electrolyte interphase characterization in lithium metal anodes. *ACS Energy Lett.* **7**, 2540–2546 (2022).
56. Yao, Y. X. et al. Regulating interfacial chemistry in lithium ion batteries by a weakly solvating electrolyte. *Angew. Chem. Int. Ed.* **60**, 4090–4097 (2021).
57. Xu, K. Non-aqueous liquid electrolytes for lithium-based rechargeable batteries. *Chem. Rev.* **104**, 4303–4417 (2004).
58. Kaminski, G. A., Friesner, R. A., Tirado-Rives, J. & Jorgensen, W. L. Evaluation and reparametrization of the OPLS-AA force field for proteins via comparison with accurate quantum chemical calculations on peptides. *J. Phys. Chem. B* **105**, 6474–6487 (2001).

59. Canongia Lopes, J. N. et al. Potential energy landscape of bis(fluorosulfonyl)amide. *J. Phys. Chem. B* **112**, 9449–9455 (2008).
60. Neese, F., Wennmohs, F., Becker, U. & Riplinger, C. The ORCA quantum chemistry program package. *J. Chem. Phys.* **152**, 224108 (2020).
61. Lu, T. & Chen, F. Multiwfn: a multifunctional wavefunction analyzer. *J. Comput. Chem.* **33**, 580–592 (2012).
62. Michaud-Agrawal, N., Denning, E. J., Woolf, T. B. & Beckstein, O. MDAAnalysis: a toolkit for the analysis of molecular dynamics simulations. *J. Comput. Chem.* **32**, 2319–2327 (2011).

Acknowledgements

S.T.O. acknowledges support from the TomKat Center Fellowship for Translational Research at Stanford University. D.T.B. acknowledges the National Science Foundation Graduate Research Fellowship Program for funding. Z.H. acknowledges support from an American Association of University Women International Fellowship. The battery and electrolyte measurement parts were supported by the Assistant Secretary for Energy Efficiency and Renewable Energy, Office of Vehicle Technologies, of the U.S. Department of Energy under the Battery Materials Research Program and the Battery500 Consortium programme. Part of this work was performed at the Stanford Nano Shared Facilities. We acknowledge J. Nelson Weker for fruitful discussions on X-ray scattering experiments.

Author contributions

S.C.K. and J.W. contributed equally. S.C.K. and Y. Cui conceived and designed the investigation. S.C.K. conducted materials synthesis and electrochemical performance testing. J.W. conducted MD simulations. R.X. conducted multiphysics simulations. P.Z. and Z.H. conducted X-ray scattering experiments. Y. Chen conducted DOSY-NMR experiments. Y. Yang conducted SEM characterizations. Z.Y. conducted electrolyte solvent synthesis. Z.H. conducted viscosity characterization. S.T.O. and L.C.G. conducted XPS

characterization. S.C.K. conducted solvation measurements. W.Z., P.S., M.S.K., D.T.B. and Y. Ye assisted with interpretation of results. J.Q., Z.B. and Y. Cui supervised the project. S.C.K., J.W. and Y. Cui co-wrote the paper. All authors discussed the results and commented on the paper.

Competing interests

The authors declare no competing interests.

Additional information

Supplementary information The online version contains supplementary material available at <https://doi.org/10.1038/s41560-023-01280-1>.

Correspondence and requests for materials should be addressed to Yi Cui.

Peer review information *Nature Energy* thanks Faezeh Makhlooghiyazad, Xiqian Yu and the other, anonymous, reviewer(s) for their contribution to the peer review of this work.

Reprints and permissions information is available at www.nature.com/reprints.

Publisher's note Springer Nature remains neutral with regard to jurisdictional claims in published maps and institutional affiliations.

Springer Nature or its licensor (e.g. a society or other partner) holds exclusive rights to this article under a publishing agreement with the author(s) or other rightsholder(s); author self-archiving of the accepted manuscript version of this article is solely governed by the terms of such publishing agreement and applicable law.

© The Author(s), under exclusive licence to Springer Nature Limited 2023